Radiation Measurements 191 (2026) 107599

Contents lists available at ScienceDirect

Radiation Measurements

journal homepage: www.elsevier.com/locate/radmeas

Optimized quantitative indirect neutron radiography method for 2D non-primary radiation measurement in BNCT

Jialong Yang [a], Xingyan Liu [b], Diyun Shu [b,*], Changran Geng [a,c,**], Xiaobin Tang [a,c], Yuan-Hao Liu [a,b]

[a] Department of Nuclear Science and Technology, Nanjing University of Aeronautics and Astronautics, Nanjing, Jiangsu Province, 210016, People's Republic of China
[b] Neuboron Therapy System Ltd., Xiamen, Fujian Province, 361000, People's Republic of China
[c] Key Laboratory of Advanced Nuclear Technology and Radiation Protection, Ministry of Industry and Information Technology, Nanjing, Jiangsu Province, 210016, People's Republic of China

ARTICLE INFO

Keywords:
Non-primary radiation
BNCT
Indirect neutron radiography
2D reaction rate

ABSTRACT

Accurate quantitative measurement of neutron non-primary radiation is crucial for the safe implementation of boron neutron capture therapy (BNCT), yet such measurement faces challenges including large measurement area and strong γ-ray interference. Indirect neutron radiography (INR) offers advantages for large-area measurement and γ resistance, but its application is limited by the low sensitivity of activation detectors and measurement errors from crosstalk. To address these challenges, dysprosium (Dy) was selected as the activation detector to enhance sensitivity, establishing a quantitative calibration relationship between its activity and imaging plate (IP) signals. For signal crosstalk during foil exposure, spatial convolution kernel was constructed using Monte Carlo simulations, and then applied with the Biconjugate Gradient Stabilized (Bi-CGSTAB) algorithm to perform spatial deconvolution of dose deposition on the IP, thereby reconstructing the actual activity of each pixel on the foil. Validation experiments demonstrated significant improvement, and the proportion of data points exceeding 5 % deviation decreased from over 60 % before correction to below 15 % after correction. Applied to clinical BNCT device, it successfully obtained the two-dimensional (2D) distribution of neutron non-primary radiation within 150–550 mm from the radiation field edge. The converted maximum skin absorbed dose rate was 1.26×10^{-4} Gy/s, located at 150 mm from the radiation field edge and decaying rapidly with increasing distance. This study achieved the quantitative measurement of 2D neutron non-primary radiation distribution in clinical BNCT devices, and provided technical support for comprehensive assessment of radiation risks and optimization of protection design.

1. Introduction

Boron Neutron Capture Therapy (BNCT) delivers a tumor-targeting boron-10 drug and then irradiates the tumor site with an external epithermal neutron beam. This triggers the $^{10}B(n, \alpha)^{7}Li$ reaction, producing high-LET particles that kill tumor cells within a very short range (Dymova et al., 2020). Consequently, BNCT achieves highly selective tumor destruction with a steep dose gradient, sparing surrounding healthy tissue (Barth and Grecula, 2020). Capitalizing on these unique technical advantages, BNCT has developed rapidly in recent years, driving the proliferation of accelerator-based BNCT (AB-BNCT) centers (Kiyanagi et al., 2019; Capoulat et al., 2025). Neutron beam characterization is fundamental for all neutron applications, including BNCT, neutron radiography (NR) (Dastjerdi et al., 2025), and prompt gamma neutron activation analysis (PGNAA) (Jafari, M et al., 2025). Particularly for BNCT beams intended for medical use, rigorous and comprehensive characterization is essential (Postuma et al., 2021). Although characterization efforts have primarily assessed in-field parameters, quantifying out-of-field non-primary radiation is critically important due to its potential to compromise the safety of healthy tissues in patient (Kakino et al., 2024).

Non-primary radiation refers to radiation emitted from medical

* Corresponding author.
** Corresponding author. Department of Nuclear Science and Technology, Nanjing University of Aeronautics and Astronautics, Nanjing, Jiangsu Province, 210016, People's Republic of China.
E-mail addresses: shudiyun@neuboron.com (D. Shu), gengchr@nuaa.edu.cn (C. Geng).

https://doi.org/10.1016/j.radmeas.2025.107599
Received 20 August 2025; Received in revised form 27 October 2025; Accepted 18 December 2025
Available online 18 December 2025

device equipment that is not intended to treat the patient. In BNCT, non-primary radiation originates from neutron and photon leakage outside the irradiation field of beam shaping assembly (BSA) and collimator. This radiation delivers non-therapeutic doses to patients, entailing unnecessary health risks (Zhang et al., 2019; McBride and Schaue, 2020). Prior to the clinical deployment of a BNCT system, non-primary radiation must be comprehensively quantified and evaluated to ensure that dose levels delivered to normal tissues outside the treatment field can be controlled within acceptable limits during patient irradiation. As emphasized by the IAEA in publication "Advances in Boron Neutron Capture Therapy", the measurements of non-primary radiation should be incorporated into relevant standards (IAEA, 2023).

Compared to photon non-primary radiation, the measurement of neutron non-primary radiation presents greater challenges. Current technologies for quantifying neutron non-primary radiation predominantly rely on offline methods such as neutron activation analysis (NAA) and thermoluminescent dosimeters (TLDs) (Tsai et al., 2018). However, these methods are inherently limited to discrete multi-point measurements. Given that comprehensive non-primary radiation assessment necessitates large-area mapping, the spatial limitations of NAA and TLDs severely restrict their application (Kry et al., 2020). To address these challenges, alternative approaches include fiber-optic scintillation detectors (Matsubayashi et al., 2021) and Gafchromic films (Hsiao and Jiang, 2019) could be viable for non-primary radiation measurement. While fiber-optic scintillation detectors offer the advantage of online measurement, their high costs and requirement for large neutron moderators restrict their applicability. The films also enable two-dimensional (2D) measurement, but they exhibit insufficient sensitivity and are susceptible to γ-ray interference in mixed radiation fields. Our team has previously developed a quantitative indirect neutron radiography (INR) method for 2D reaction rate measurement within radiation fields (Wang et al., 2024). This method offers advantages including large-area coverage, fairly high accuracy, and immunity to γ-ray interference. These features make it a promising solution for the challenges associated with neutron non-primary radiation measurement.

However, the quantitative INR method cannot be directly applied to non-primary radiation measurement at present. On the one hand, the intensity of non-primary radiation is relatively weak, and the radionuclide activity of the copper plates used in existing techniques after activation is insufficient to meet measurement requirements. On the other hand, the accuracy is lower than that of the NAA, so its accuracy needs to be further improved. The objective of this work is to further optimize the quantitative INR Method, develop metal plates more suitable for non-primary radiation measurement, improve the measurement accuracy, and apply it to the non-primary radiation measurement of BNCT device.

2. Materials and methods

2.1. Introduction of the quantitative INR method

The fundamental principle of the quantitative INR method involves first irradiating an activation detector with a neutron beam to produce radionuclides, then using an imaging plate (IP) to measure the radioactivity within the activation detector. The IP signals and dose deposition are linked through a calibration curve. Since the dose deposition is closely related to the activity of radionuclides, the 2D distribution of reaction rates in the activation detector can then be derived from the IP signals. The specific measurement procedure of the quantitative INR method is illustrated in Fig. 1.

Establishing a robust calibration curve to quantitatively correlate IP signals with dose deposition is a core challenge in quantitative INR method. Key influencing factors include the time-dependent decay of IP signals, the temperature dependence of stored IP signals, spatial inhomogeneity of signals during laser excitation readout, and the energy-dependent response of the detector. While these issues were addressed in our prior studies (Wang et al., 2024), such advancements remain insufficient to enable the application of the quantitative INR method to neutron non-primary radiation measurements. Two critical unresolved limitations persist: (1) inadequate sensitivity of the activation detector, and (2) degradation of measurement accuracy induced by signal crosstalk during exposure. To mitigate these constraints, we implemented two targeted improvements: (i) optimized material selection for the activation detector, and (ii) algorithmic correction of signal crosstalk during exposure.

2.2. Material selection of activation detector

Quantitative measurement of non-primary radiation outside the radiation field necessitates activation materials with high neutron capture cross-sections to compensate for low flux conditions. Beyond radionuclide activity, the IP signal critically depends on dose deposition per unit activity. To comprehensively evaluate material performance, the relative dose deposition coefficient D_{Rel} is defined herein as a comparison criterion:

$$D_{Rel} = A_{Rel} \cdot \sigma \tag{1}$$

where A_{Rel} is the activity normalized to the maximum among the materials and σ (unit: μGy/Bq) is the dose deposition per unit activity. D_{Rel} reflects the IP response under identical neutron spectrum and flux conditions. Four materials (Cu, Au, Dy, Mn) were preselected based on half-life of activated radionuclide, cross-section, isotopic abundance, and fabrication practicality, with full specifications detailed in Table 1.

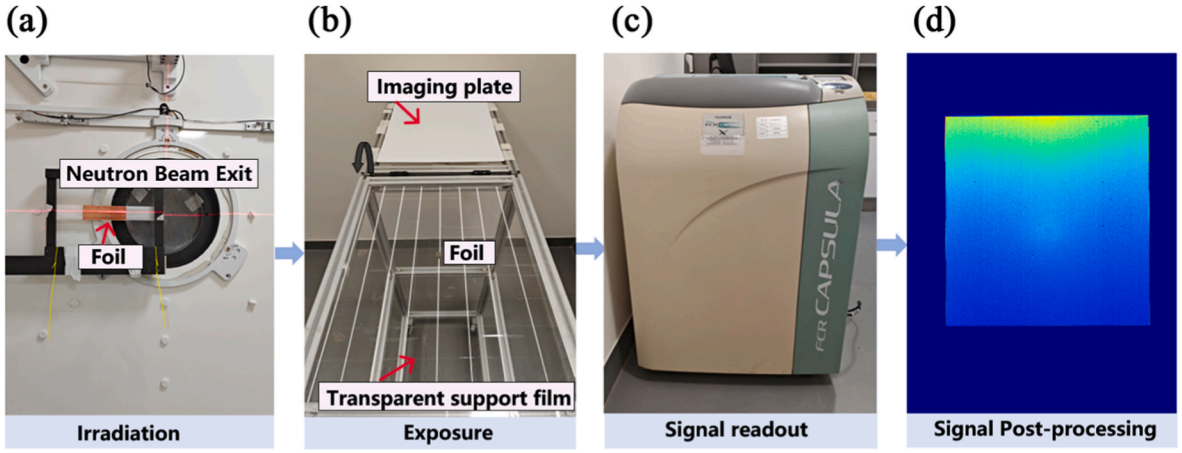

Fig. 1. Measurement procedure of the quantitative INR Method.

Table 1
Key properties of candidate activation detector materials.

Materials	Target nuclides	Natural abundance (%)	Nuclear reaction	Half-life
Cu	^{63}Cu	69.15	^{63}Cu (n, γ)^{64} Cu	12.70 h
Au	^{197}Au	100	^{197}Au (n, γ)^{198}Au	2.27 d
Dy	^{164}Dy	28.26	^{164}Dy (n, γ)^{165}Dy	2.33 h
Mn	^{55}Mn	100	^{55}Mn (n, γ)^{56}Mn	2.58 h

Their post-activation radioactivity in the non-primary radiation region (150–350 mm from BSA exit) was simulated using PHITS (Version 3.28) (Furuta and Sato, 2021) with the source model of NeuPex system.

Dose deposition per unit activity was further simulated via the model in Fig. 2, where the foil has a diameter of 12.6 mm and a thickness of 0.5 mm. Decay spectra of radionuclides were obtained from the ENDF/B-VIII.0 database (Shibata et al., 2011; Brown et al., 2018). For each simulation, the average dose deposition was calculated over a 15 × 15 pixels region (pixel size: 0.2 mm × 0.2 mm) directly below the foil. Averaging across this extended area effectively reduces statistical uncertainties inherent in Monte Carlo simulations while minimizing contributions from inter-source crosstalk.

2.3. Calibration curve between IP signal and dose deposition

A calibration curve correlating IP signal with dose deposition was established using standardized metal foils (diameter: 12.6 mm, thickness: 0.5 mm). Identical foil groups were neutron-irradiated for distinct durations of 15 and 25 min. The resultant radionuclide activities were quantified using a High-Purity Germanium (HPGe) detector, with each foil measured three times to reduce systematic errors. Each activated foil was then exposed to an IP for systematically varied intervals. The dose deposition during each exposure was calculated from the radionuclide activity of foil, dose deposition per unit activity, and the exposure duration. This procedure generated 23 calibration data points, with exposure times spanning 30 s to 40 min.

2.4. Correction method of decay particles crosstalk during exposure

When exposing the metal foil on IP, the signal measured at each pixel should ideally correspond only to the radioactivity of foil area directly above it. However, as depicted in Fig. 3(a), decay particles from adjacent foil regions also contribute to the signal of the target IP pixel in practice. Consequently, dedicated signal processing and reconstruction are required to recover the true local activity distribution.

The imaging of an activated metal plate exposed on the IP can be considered a convolution process (Kuo, 2016). When the foil and IP are divided into pixels measuring 0.2 mm × 0.2 mm, the signal measured at each IP pixel results from spatial integration of radioactivity within a surrounding local region of the foil. Let A_{ij} denote the activity at foil pixel (i, j) and D_{ij} represent the corresponding dose deposition measured at IP pixel (i, j). As the convolution kernel w scans across the activity distribution A_{ij}, the resulting output at each IP pixel corresponds to D_{ij}. Consequently, defining the relationship between dose deposition and activity is critically determined by the kernel w. As illustrated in Fig. 3 (c), the foil was divided into a grid of $u \times v$ pixels to simulate the dose contribution of decay particles from each foil pixel to the target IP pixel. Considering computational efficiency, contributions beyond the n-th pixel ring were deemed negligible when their cumulative contribution fell below 1 % of the directly-above-foil contribution. This yielded a convolution kernel $w[u,v]$ with dimensions $u \times v = 15 \times 15$. Subsequent convolution over the foil domain with stride 1 established an equation for each pixel, thus yielding the linear system given in Equation (2) with i × j equations and i × j unknowns. When $i + m$ - $(u+1)/2$ or $j + n$ - $(v+1)/2$ falls outside the range of matrix A, the boundary is supplemented using Equation (3), where H and W denote the height and width of matrix A respectively.

$$\begin{cases} D_{(1,1)} = \int_0^T \sum_{m=1}^{u}\sum_{n=1}^{v} A\left[1+m-\left(\frac{u+1}{2}\right), 1+n-\left(\frac{v+1}{2}\right)\right]\cdot w[m,n] \\ D_{(1,2)} = \int_0^T \sum_{m=1}^{u}\sum_{n=1}^{v} A\left[1+m-\left(\frac{u+1}{2}\right), 2+n-\left(\frac{v+1}{2}\right)\right]\cdot w[m,n] \\ \cdots\cdots \\ D_{(i-1,j-1)} = \int_0^T \sum_{m=1}^{u}\sum_{n=1}^{v} A\left[i-1+m-\left(\frac{u+1}{2}\right), j-1+n-\left(\frac{v+1}{2}\right)\right]\cdot w[m,n] \\ \cdots\cdots \\ D_{(i,j)} = \int_0^T \sum_{m=1}^{u}\sum_{n=1}^{v} A\left[i+m-\left(\frac{u+1}{2}\right), j+n-\left(\frac{v+1}{2}\right)\right]\cdot w[m,m] \end{cases} \tag{2}$$

$$A_{pad}[i,j] = \begin{cases} A[i,j] & if\ 1 \le i \le H, 1 \le j \le W \\ 0 & otherwise \end{cases} \tag{3}$$

The resulting linear system was solved using the Biconjugate Gradient Stabilized (Bi-CGSTAB) algorithm (Sleijpen et al., 1994), chosen for its rapid convergence with asymmetric systems and efficiency for large-scale sparse matrices. The theoretical basis of this algorithm is established in Vorst H.'s seminal work (Van der Vorst, 1992). Through extensive testing, the maximum iteration count was fixed at 2000 with a convergence tolerance of 1×10^{-10}, terminating when either threshold was satisfied. This yielded the corrected activity distribution across all pixels.

2.5. Validation of the crosstalk calibration for INR method

To validate the effectiveness of the crosstalk calibration methodology, two sets of comparative experiments were designed. Two Dy foils (3 cm × 10 cm × 0.05 cm) were mounted within a polymethyl methacrylate (PMMA) phantom and irradiated at the epithermal neutron beam of the NeuPex system, as shown in Fig. 4. Post-irradiation, 2D reaction rate distributions pre- and post-crosstalk correction were obtained via the INR method, followed by comparative analysis with NAA results.

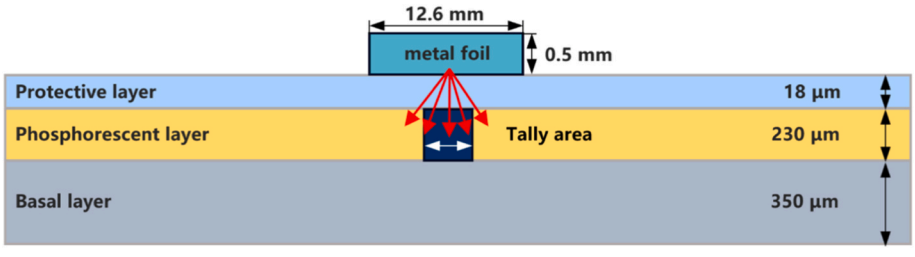

Fig. 2. Computational framework for dose deposition from activated foil to IP phosphor layer.

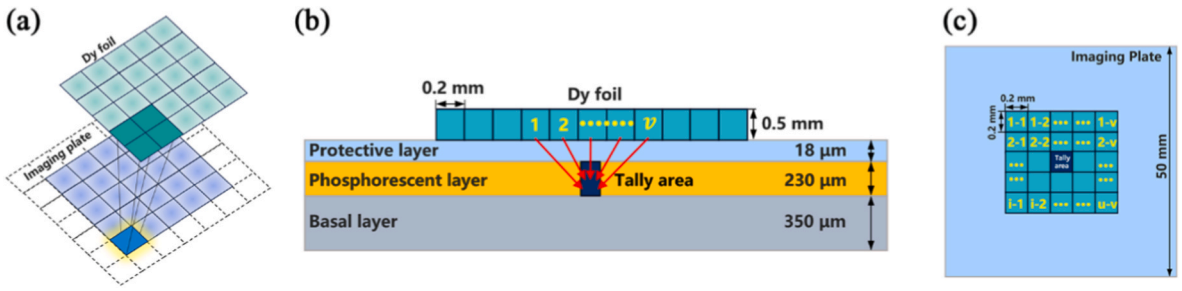

Fig. 3. Schematic of the correction method for decay particle crosstalk. (a) Conceptual representation of decay particle crosstalk. (b) Side view of the computational model for convolution kernel. (c) Top view of the computational model for convolution kernel.

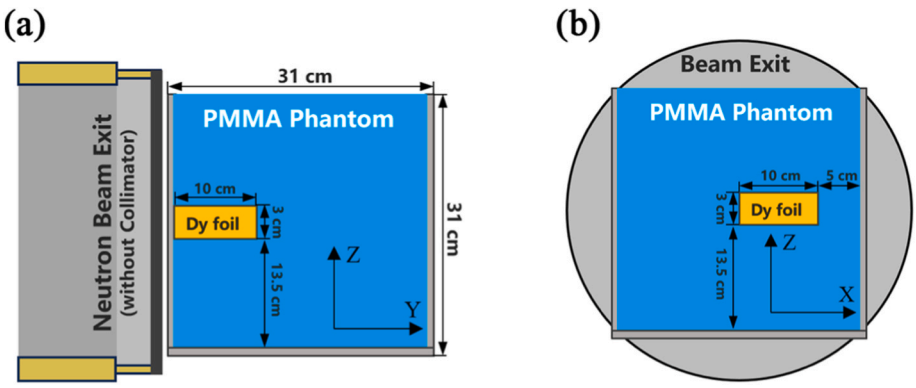

Fig. 4. Experimental configuration of the Dy foil embedded within a PMMA phantom. (a) Dy foil aligned parallel to the beam center axis. (b) Dy foil aligned perpendicular to the beam center axis.

The phantom features 0.5-cm-thick sidewalls, a 1-cm-thick base, and an internal volume of 30 × 30 × 30 cm^3 filled with stacked PMMA slabs. The PMMA phantom was placed directly against the beam exit, with its central axis precisely aligned to the beam central axis. One Dy foil was positioned along the central beam axis at depths ranging from 0.5 cm to 10.5 cm. The other Dy foil was positioned perpendicularly to the central beam axis at a depth of 2.8 cm. Its alignment extends from the central beam axis to a lateral position 10 cm away. Both foils were irradiated for 5 min and cooled for 4 h before exposure. Following exposure, each foil was sectioned into three uniform strips measuring 1 cm × 10 cm × 0.05 cm. The central strip was then subdivided into 1 cm × 0.5 cm segments. These segments underwent activity measurement via an HPGe detector. As the measurement error of NAA is generally within 5 % (Kafala and MacMahon, 2007), it can serve as a reference standard.

2.6. 2D non-primary radiation measurement of BNCT beam

IEC standards require non-primary radiation measurements to be performed in the patient plane at positions ranging from 150 mm to 2000 mm from the radiation field edge. However, there is currently no clearly defined concept of the patient plane and radiation field in BNCT. In this study, the peak depth of thermal neutron flux within the PMMA phantom is defined as the patient plane, and the geometry of the beam exit is designated as the radiation field.

Non-primary radiation measurements were performed on the epithermal neutron beam of the NeuPex accelerator-based BNCT system (developed by Neuboron Medical Group). The system has been installed at Xiamen Humanity Hospital and is now undergoing clinical trials. Under proton beam conditions of 2.35 MeV and 10 mA, the epithermal neutron flux at the exit exceeds 1 × 10^9 n/cm^2·s^{-1}. This study will also be conducted under these clinical nominal conditions. Measurements were conducted employing a large-area foil of dimensions 20 cm × 20 cm × 0.05 cm. The foil was positioned 2.8 cm from the beam exit via a robotic arm and support fixture, ensuring the horizontal alignment of the foil centerline with the central axis of the beam. Due to limitations of the foil specifications, the continuous reaction rate distribution in the region 150–550 mm from the radiation field edge was obtained by splicing two measurement results: the 150–350 mm region irradiated for 35 min and the 350–550 mm region irradiated for 45 min, with spatial configurations detailed in Fig. 5. Post-irradiated foils were cooled for 25 min, then received consecutive 35, 45, and 60-min exposures to reduce measurement uncertainty. The IP signal with the optimal signal-to-noise ratio was selected for convolution correction, enabling pixel-wise quantification of the actual 2D reaction rate.

In the assessment of non-primary radiation, the ratio of the maximum dose at distances ranging from 150 mm to 2000 mm from the field edge to the dose delivered to the patient within the treatment field is typically evaluated. This dose should refer to a definite quantity, such as absorbed dose, ambient dose equivalent, or personal dose equivalent. In this study, the absorbed dose was adopted for assessment, requiring the conversion of reaction rate to absorbed dose rate using weighted cross-sections (Huang and Jiang, 2017) and dose conversion coefficients (Petoussi-Henss et al., 2010). Under a specific neutron energy spectrum, the reaction rate R and absorbed dose rate $\dot{D}$ can be expressed as Equation (4) and Equation (5), respectively.

$$R = \Phi \cdot \sigma_w \tag{4}$$

$$\dot{D} = \Phi \cdot k_w \tag{5}$$

where R is reaction rate (reaction/s), $\dot{D}$ is absorbed dose rate (Gy/s), Φ is total neutron flux (n/cm^2·s^{-1}), σ_w denotes weighted cross section (cm^2), and k_w represents weighted dose conversion coefficients (Gy·cm^2). Thus, the conversion of reaction rate and absorbed dose rate can be achieved via Equation (6). Considering the non-primary radiation region, the analysis focused on the female skin absorbed dose rate under antero-posterior (AP) irradiation, which maximizes skin dose.

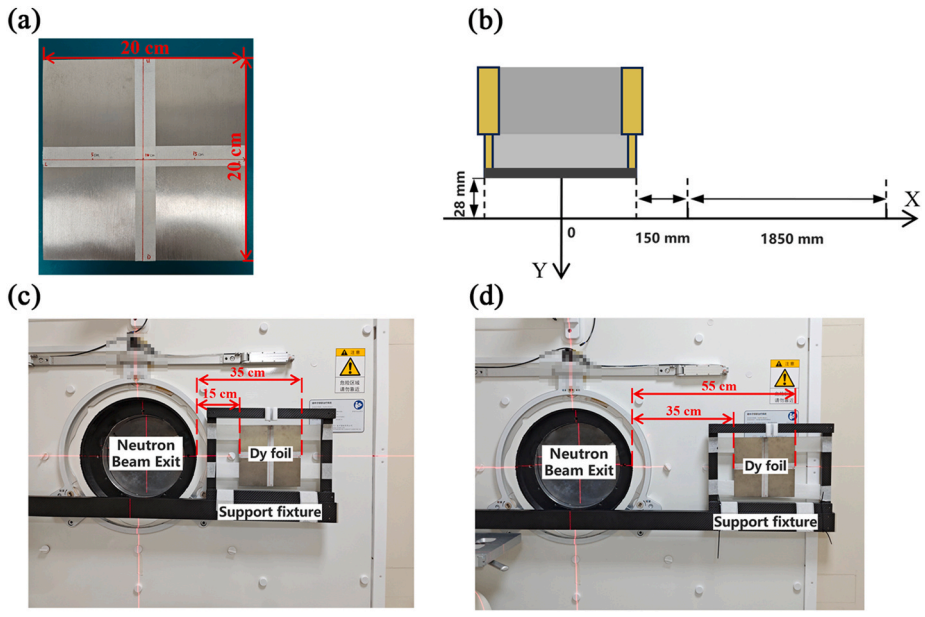

Fig. 5. Experimental configuration of non-primary radiation measurement. (a) Image of the Dy foil. (b) Top view of the measurement position for non-primary radiation. (c) Front view of foil location at 150–350 mm from radiation field edge. (d) Front view of foil location at 350–550 mm from radiation field edge.

$$\dot{D} = R \cdot \frac{k_w}{\sigma_w} \tag{6}$$

3. Result

3.1. Material selection of activation detector

Table 2 shows the normalized activities of radionuclide and dose deposition on IP for four alternative materials following non-primary radiation irradiation. The dose deposition per unit activity of Dy foil on the IP is second only to that of Mn, but its radionuclide activity is significantly higher than that of other materials, thus achieving the highest relative dose deposition coefficient. In summary, the activated product of Dy per unit area generates the highest signal intensity on the IP under non-primary irradiation conditions. Furthermore, the activated target radionuclide in the Dy material is ^{165}Dy, with a half-life of 2.331 h (Jordan et al., 1953), enabling rapid reusability. Although other radionuclides are generated synchronously, ^{165m}Dy exhibits a short half-life (1.257 min) while the contributions of ^{156}Dy and ^{158}Dy remain below 0.1 %, collectively presenting no interference to ^{165}Dy measurements. Consequently, Dy was ultimately selected as the activated detector material for non-primary radiation measurements in BNCT.

3.2. Calibration curve between IP signal and dose deposition

Fig. 6 presents 23 sets of data points for IP signal and dose deposition values. The fitting result shows that the IP signal value increases rapidly with initial dose deposition and then increases more slowly afterward. Fitting all data points yielded Equation (7) with $R^2 = 0.997$. To reduce the measurement uncertainty of IP signal values and minimize the impact of IP signal fluctuations on dose deposition, subsequent IP signal values were maintained within the approximate range of 2200–2700.

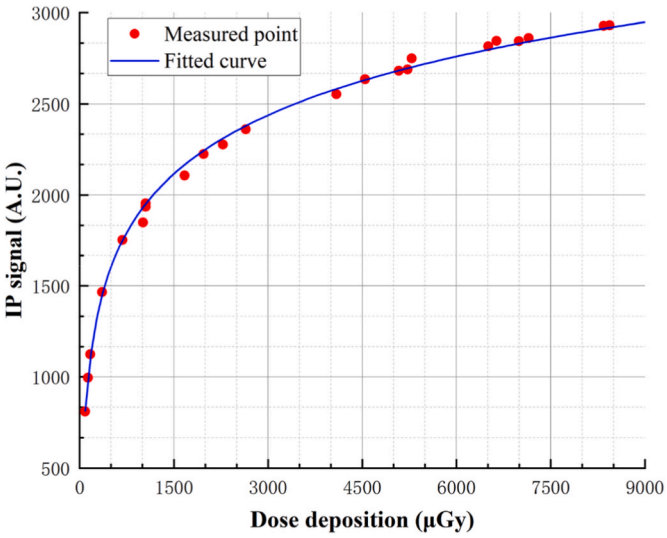

Fig. 6. Calibration curve between IP signal and dose deposition.

$$IP = 464.4614 \cdot \ln(dose) - 1281.006 \tag{7}$$

3.3. Validation of the crosstalk calibration for INR method

Fig. 7 presents the depth distribution of reaction rates, and the relative deviations between the measurements from the INR method (before and after correction) and the NAA method. Prior to crosstalk correction, relative deviations exceeding 5 % were observed at 14 positions, including five positions where deviations exceeded 10 %. Following correction, the number of positions exhibiting deviations greater than 5 % decreased significantly to three, with only one position exceeding 10 %. Fig. 8 shows the corresponding off-axis reaction rate distribution and relative deviations. Before correction, deviations exceeded 5 % at 12 positions, three of which exceeded 10 %. After

Table 2
Normalized activities and relative dose deposition coefficient of candidate materials.

Radionuclide	σ: μGy/Bq	A_{Rel}	D_{Rel}: μGy/Bq
^{165}Dy	3.459×10^{-5}	1[a]	3.459×10^{-5}
^{56}Mn	7.441×10^{-5}	1.891×10^{-2}	1.407×10^{-6}
^{64}Cu	2.461×10^{-5}	2.940×10^{-4}	7.236×10^{-9}
^{198}Au	1.192×10^{-5}	4.899×10^{-4}	5.840×10^{-9}

[a] Since the Dy foil has the highest activity among candidate materials, it serves as the normalization reference.

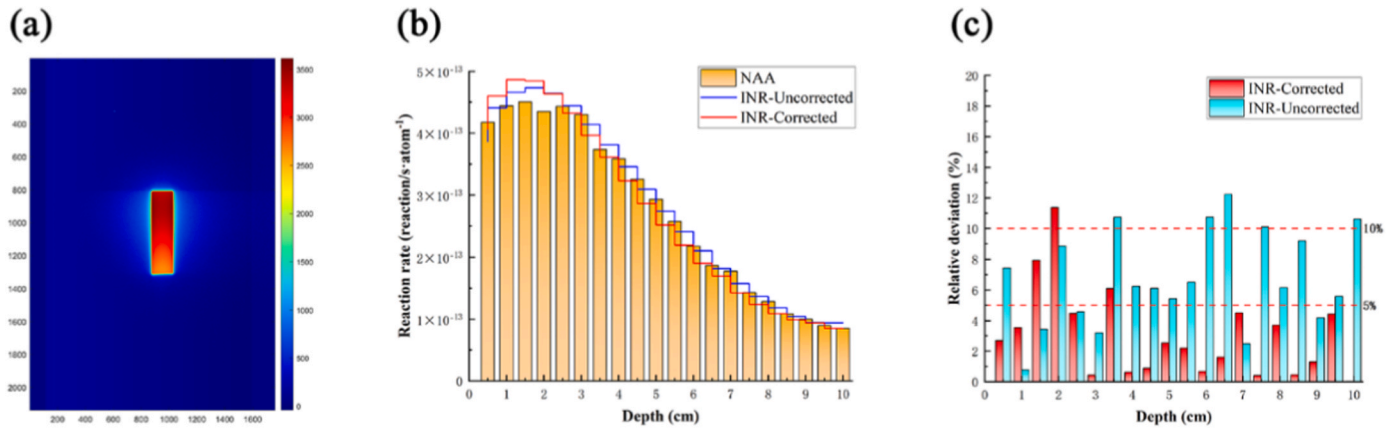

Fig. 7. Depth distribution of reaction rate measured by INR and NAA methods. (a) Image of IP signal distribution after exposure. (b) Depth distribution of reaction rate. (c) Relative deviations between INR and NAA results before and after correction.

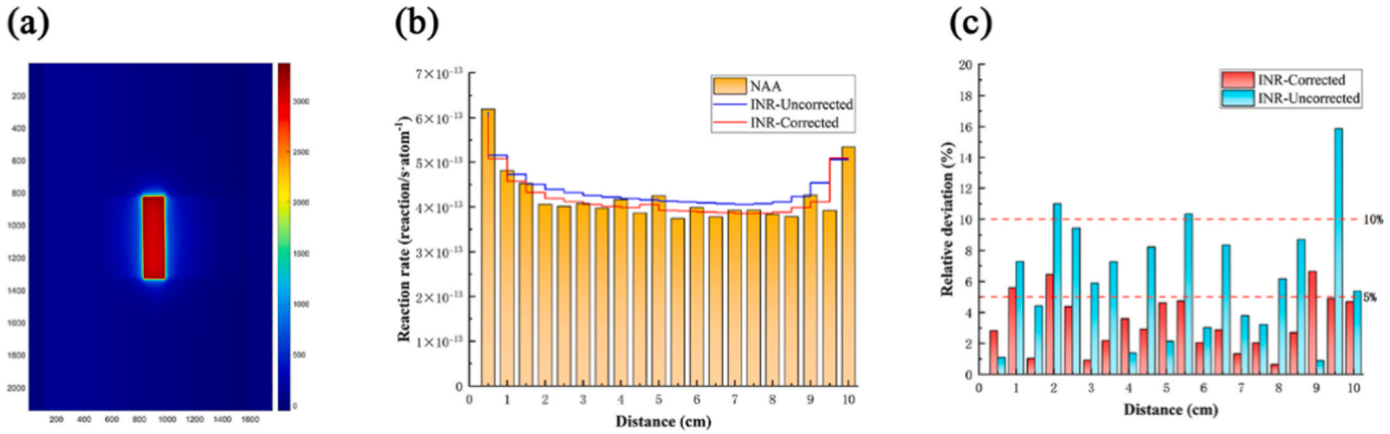

Fig. 8. Off-axis distribution of reaction rate measured by INR and NAA methods. (a) Image of IP signal distribution after exposure. (b) Off-axis distribution of reaction rate. (c) Relative deviations between INR and NAA results before and after correction.

correction, only three positions showed deviations above 5 %, and the maximum deviation was reduced to 6.65 %, demonstrating the effectiveness of the crosstalk correction.

3.4. 2D non-primary radiation measurement of BNCT beam

The 2D reaction rate distribution obtained with the optimized INR method is shown in Fig. 9(a). Applying spectrum-weighted cross-sections and dose conversion coefficients, this distribution was converted to the 2D absorbed dose rate in female skin, as presented in Fig. 9(b).

Analysis of the spatial reaction rate distribution confirmed that the optimized INR method reconstructs the actual activity of each pixel and maintains consistency across the stitching region of the two measurements. After conversion to female skin absorbed dose rate, the maximum absorbed dose rate was 1.26×10^{-4} Gy/s, occurring at 150 mm from the radiation field edge, as shown in Fig. 10(a). In the horizontal direction, the absorbed dose rate decreased rapidly with increasing distance from the radiation field edge. At 550 mm, the maximum absorbed dose rate was only 9.98×10^{-6} Gy/s, so subsequent regions were not measured further. Fig. 10(b) shows that within 300 mm from the radiation field edge, the dose rate at the central point in the vertical direction was the highest and decreased with increasing radial distance. Beyond 300 mm, the overall neutron flux remained at a relatively low level, and the variation of dose rate in the radial region tended to stabilize. Therefore,

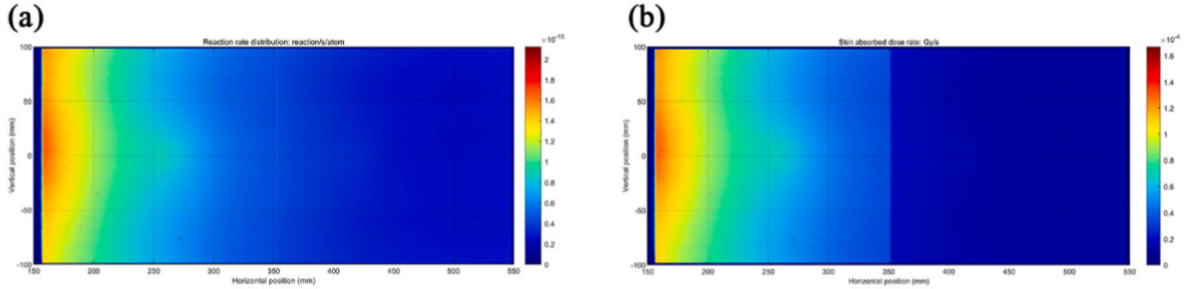

Fig. 9. Non-primary radiation data measured within 150–550 mm from the radiation field edge. (a) 2D distribution of reaction rate in the 150–550 mm region. (b) Converted 2D distribution of female skin absorbed dose rate under AP irradiation in the 150–550 mm region.

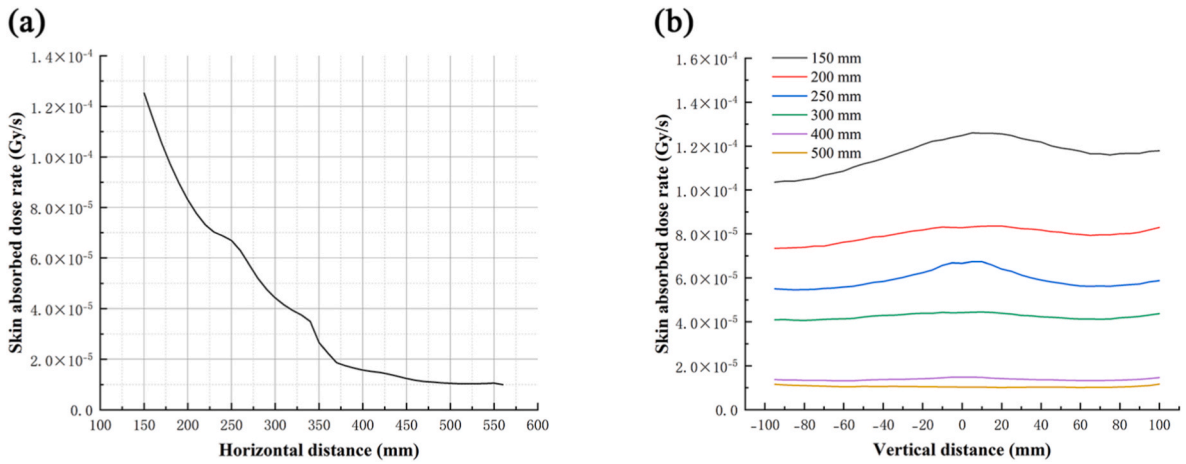

Fig. 10. Distribution of absorbed dose rate in female skin at horizontal and vertical positions. (a) Variation of absorbed dose rate with horizontal distance at the beam center height. (b) Variation of absorbed dose rate with vertical height at different horizontal positions.

the evaluation of non-primary radiation can be conducted in the central region of the vertical direction.

4. Discussion

Experimental verification demonstrated that correction for crosstalk significantly enhances the measurement accuracy of the quantitative INR method. Following optimization, the average relative deviation in reaction rates between the INR method and HPGe detector measurements within the PMMA phantom decreased to approximately 3 %. Local deviations exceeding 10 % were primarily attributed to indentations of the foil, leading to deviations between the actual dose deposition and simulated values. Future studies could use flatter foils or mitigate this error type through signal compensation techniques.

Notably, experiments found an abnormal increase in reaction rate at both ends of Dy foil placed perpendicular to the center beam axis, which is inconsistent with the theoretical expectation of neutron flux attenuation with distance. This phenomenon may be attributed to unreacted neutrons in the blank area outside the foil scattering to the edge, thereby increases the local neutron flux, and the same result was also observed in simulations. When Dy foil is placed parallel to the beam, beam depth attenuation dominates the distribution, with no such anomalies occurring. This mechanism suggests that for in-phantom measurements, the gap between the foil and the phantom should be minimized or thin foils ($<$0.01 cm) should be used to suppress scattering interference.

Compared to in-phantom measurements, non-primary radiation measurements in air face additional limitations primarily from environmental scattering interference. As shown in Fig. 9(b), the inhomogeneity of scattering field in the treatment room causes an abrupt change in the dose rate distribution at the measurement splicing position. Although the experiment minimized scattering from the robotic arm by measuring on the right side of the BSA, support fixture still exerted observable effects on regions adjacent to the foil edges, resulting in a trend where the dose rate in the 0–100 mm radial range first decreases and then increases. To improve global measurement accuracy, a complete scattering correction model including walls, robotic arms, and brackets needs to be developed in the future.

Based on the acquired measurement data, the current dose conversion using female skin under AP irradiation is intuitive. The converted dose provides a simplified estimate but neglects the effects of actual radiation incidence angles, energy spectrum gradients, and tissue heterogeneity present during treatment, which may lead to overestimation or underestimation of dose. Consequently, the next step involves establishing a generalized conversion relationship from measurable quantities to organ doses using anthropomorphic phantoms. This will provide a more robust foundation for developing non-primary radiation protection standards.

While quantitative INR method offers higher measurement accuracy and improved efficiency over previous offline techniques, the entire process may still take several hours. Given practical needs, a real-time online measurement approach would be highly desirable in the future. However, realizing this will likely require solving the issue of γ-ray interference, potentially through Monte Carlo correction or the use of appropriate shielding materials. Successfully addressing the gamma contribution would allow the direct method to be applied to neutron non-primary radiation measurements, significantly simplifying the operational workflow. This direction will be further explored in future work.

5. Conclusion

Addressing the challenges of accurate measurement of neutron non-primary radiation, this study significantly optimized the quantitative INR method by adapting high-sensitivity activation detectors and developing innovative source crosstalk correction method. Measurements on clinical AB-BNCT devices based on this method revealed that high-dose regions of non-primary radiation are concentrated in the central region in the vertical direction and decay rapidly with increasing horizontal distance. Importantly, at 150 mm from the radiation field edge, a 30-min irradiation can cause the absorbed dose to the skin outside the radiation field to reach 0.227 Gy. This dose level highlights the impact of non-primary radiation on sensitive tissues, necessitating systematic evaluation. This study has achieved the quantitative measurement of the 2D distribution of BNCT neutron non-primary radiation, demonstrating the feasibility of the optimized INR method. By balancing precision and efficiency, this approach provides an effective tool for comprehensive non-primary radiation assessment.

CRediT authorship contribution statement

Jialong Yang: Writing – original draft, Data curation, Conceptualization. **Xingyan Liu:** Writing – review & editing, Methodology, Conceptualization. **Diyun Shu:** Writing – review & editing, Supervision, Methodology, Funding acquisition, Formal analysis. **Changran Geng:** Writing – review & editing, Supervision, Methodology. **Xiaobin Tang:** Writing – review & editing. **Yuan-Hao Liu:** Writing – review & editing.

Declaration of competing interest

The authors declare that they have no known competing financial

interests or personal relationships that could have appeared to influence the work reported in this paper.

Acknowledgments

This work is supported by the National Key Research and Development Program of China (Grant No.2023YFE0197700) and the National Natural Science Foundation of China (Grant No.12261131621, 12220101005).

Data availability

Data will be made available on request.

References

Brown, D.A., Chadwick, M.B., Capote, R., Kahler, A.C., Trkov, A., Herman, M.W., et al., 2018. ENDF/B-VIII. 0: the 8th major release of the nuclear reaction data library with CIELO-project cross sections, new standards and thermal scattering data. Nucl. Data Sheets 148, 1–142. https://doi.org/10.1016/j.nds.2018.02.001.

Barth, R.F., Grecula, J.C., 2020. Boron neutron capture therapy at the crossroads-where do we go from here? Appl. Radiat. Isot. 160, 109029. https://doi.org/10.1016/j.apradiso.2019.109029.

Capoulat, M.E., Cartelli, D., Baldo, M., Sandín, J.S., Del Grosso, M.F., Bertolo, A., et al., 2025. Accelerator based-BNCT facilities worldwide and an update of the Buenos Aires project. Appl. Radiat. Isot. 219, 111723. https://doi.org/10.1016/j.apradiso.2025.111723.

Dastjerdi, M.C., Jafari, M., Mokhtari, J., Jafari, H., 2025. Optimization of neutron radiography using machine learning and genetic algorithm for boron concentration measurement. Nucl. Instrum. Methods Phys. Res. Sect. A Accel. Spectrom. Detect. Assoc. Equip., 171030 https://doi.org/10.1016/j.nima.2025.171030.

Dymova, M.A., Taskaev, S.Y., Richter, V.A., Kuligina, E.V., 2020. Boron neutron capture therapy: current status and future perspectives. Cancer Commun. 40 (9), 406–421. https://doi.org/10.1002/cac2.12089.

Furuta, T., Sato, T., 2021. Medical application of particle and heavy ion transport code system PHITS. Radiol. Phys. Technol. 14 (3), 215–225. https://doi.org/10.1007/s12194-021-00628-0.

Huang, C.K., Jiang, S.H., 2017. Neutron activation analysis using a modified absolute calibration method. J. Radioanal. Nucl. Chem. 311 (2), 1201–1207. https://doi.org/10.1007/s10967-016-5135-4.

Hsiao, M.C., Jiang, S.H., 2019. In-phantom neutron dose measurement using Gafchromic film dosimeter for QA of BNCT beams. Appl. Radiat. Isot. 143, 79–86. https://doi.org/10.1016/j.apradiso.2018.09.030.

INTERNATIONAL ATOMIC ENERGY AGENCY, 2023. Advances in Boron Neutron Capture Therapy, Non-serial Publications. IAEA, Vienna.

Jafari, M., Jafari, H., Dastjerdi, M.C., Mokhtari, J., 2025. Characterization of the PGNAA neutron beam of Isfahan MNSR through the calculations and different measurement methods. Measurement 241, 115704. https://doi.org/10.1016/j.measurement.2024.115704.

Jordan, W.C., Cork, J.M., Burson, S.B., 1953. Decay of Dy 1 6 5 m 66 (1.2 min) and Dy 165 66 (2.3 hr). Phys. Rev. 92 (5), 1218. https://doi.org/10.1103/PhysRev.92.1218.

Kafala, S.I., MacMahon, T.D., 2007. Comparison of neutron activation analysis methods. J. Radioanal. Nucl. Chem. 271 (2), 507–516. https://doi.org/10.1007/s10967-007-0238-6.

Kuo, C.C.J., 2016. Understanding convolutional neural networks with a mathematical model. J. Vis. Commun. Image Represent. 41, 406–413. https://doi.org/10.1016/j.jvcir.2016.11.003.

Kiyanagi, Y., Sakurai, Y., Kumada, H., Tanaka, H., 2019. Status of accelerator-based BNCT projects worldwide. AIP Conf. Proc. 2160 (1), 050012. https://doi.org/10.1063/1.5127704. AIP Publishing LLC.

Kry, S.F., Alvarez, P., Cygler, J.E., DeWerd, L.A., Howell, R.M., Meeks, S., et al., 2020. AAPM TG 191: clinical use of luminescent dosimeters: TLDs and OSLDs. Med. Phys. 47 (2), e19–e51. https://doi.org/10.1002/mp.13839.

Kakino, R., Hu, N., Tanaka, H., Takeno, S., Aihara, T., Nihei, K., Ono, K., 2024. Out-of-field dosimetry using a validated PHITS model and computational phantom in clinical BNCT. Med. Phys. 51 (2), 1351–1363. https://doi.org/10.1002/mp.16916.

McBride, W.H., Schaue, D., 2020. Radiation-induced tissue damage and response. J. Pathol. 250 (5), 647–655. https://doi.org/10.1002/path.5389.

Matsubayashi, N., Tanaka, H., Takata, T., Okazaki, K., Sakurai, Y., Suzuki, M., 2021. Development of real-time neutron detectors with different sensitivities to thermal, epithermal, and fast neutrons in BNCT. Radiat. Meas. 140, 106489. https://doi.org/10.1016/j.radmeas.2020.106489.

Petoussi-Henss, N., Bolch, W.E., Eckerman, K.F., Endo, A., Hertel, N., Hunt, J., et al., 2010. Conversion coefficients for radiological protection quantities for external radiation exposures. Ann. ICRP 40 (2–5), 1–257. https://doi.org/10.1016/j.icrp.2011.10.001.

Postuma, I., González, S., Herrera, M.S., Provenzano, L., Ferrarini, M., Magni, C., et al., 2021. A novel approach to design and evaluate BNCT neutron beams combining physical, radiobiological, and dosimetric figures of merit. Biology 10 (3), 174. https://doi.org/10.3390/biology10030174.

Sleijpen, G.L., Van der Vorst, H.A., Fokkema, D.R., 1994. BiCGstab (l) and other hybrid Bi-CG methods. Numer. Algorithms 7 (1), 75–109. https://doi.org/10.1007/BF02141261.

Shibata, K., Iwamoto, O., Nakagawa, T., Iwamoto, N., Ichihara, A., Kunieda, S., et al., 2011. JENDL-4.0: a new library for nuclear science and engineering. J. Nucl. Sci. Technol. 48 (1), 1–30. https://doi.org/10.1080/18811248.2011.9711675.

Tsai, W.C., Huang, C.K., Jiang, S.H., 2018. QA measurement of gamma-ray dose and neutron activation using TLD-400 for BNCT beam. Appl. Radiat. Isot. 137, 73–79. https://doi.org/10.1016/j.apradiso.2018.03.010.

Van der Vorst, H.A., 1992. Bi-CGSTAB: a fast and smoothly converging variant of Bi-CG for the solution of nonsymmetric linear systems. SIAM J. Sci. Stat. Comput. 13 (2), 631–644. https://doi.org/10.1137/0913035.

Wang, X., Shu, D., Geng, C., Tang, X., Liu, Y.H., 2024. Advancing 2D reaction rate measurements in BNCT: validation of the indirect neutron radiography method. Radiat. Meas. 174, 107133. https://doi.org/10.1016/j.radmeas.2024.107133.

Zhang, X., Geng, C., Tang, X., Bortolussi, S., Shu, D., Gong, C., et al., 2019. Assessment of long-term risks of secondary cancer in paediatric patients with brain tumours after boron neutron capture therapy. J. Radiol. Prot. 39 (3), 838. https://doi.org/10.1088/1361-6498/ab29a3.